Standing-Wave and RF Penetration Artifacts Caused by Elliptic Geometry: An Electrodynamic Analysis of MRI

John G. Sled* and G. Bruce Pike, *Member, IEEE*

Abstract— **Motivated by the observation that the diagonal pattern of intensity nonuniformity usually associated with linearly polarized radio-frequency (RF) coils is often present in neurological scans using circularly polarized coils, a theoretical analysis has been conducted of the intensity nonuniformity inherent in imaging an elliptically shaped object using 1.5-T magnets and circularly polarized RF coils. This first principle analysis clarifies, for the general case of conducting objects, the relationship between the excitation field and the reception sensitivity of circularly and linearly polarized coils. The results, validated experimentally using a standard spin-echo imaging sequence and an *in vivo* B_1 field mapping technique, are shown to be accurate to within 1%–2% root mean square, suggesting that these electromagnetic interactions with the object account for most of the intensity nonuniformity observed.**

Index Terms— **Intensity nonuniformity, magnetic resonance imaging, RF field inhomogeneity, shading artifact.**

I. Introduction

INTENSITY nonuniformity is the smooth intensity variation often seen in magnetic resonance images (MRI's) caused by such factors as inhomogeneous radio-frequency (RF) excitation [1], nonuniform reception coil sensitivity, eddy currents driven by field gradients [2], as well as the electrodynamic interactions with the object often described as RF penetration and standing-wave effects [3]. In modern MRI scanners using circularly polarized head or body coils that produce nominally uniform fields, these variations are often subtle enough that they are difficult to detect by visual inspection. However, the increasing use of automatic segmentation techniques, which assume homogeneity of intensity within each tissue class, has driven interest in correcting this artifact [4]–[8], as it can significantly degrade their performance.

A number of authors have conducted theoretical analyzes of the excitation field (B_1) and reception sensitivity variations that contribute to image intensity nonuniformity. This kind of analysis is greatly simplified by treating the excitation field as static and using the Biot–Savart law to compute magnetic field strength by integrating the contributions of nearby currents [1], [9]. While this approach simplifies the modeling of complicated coil shapes, it neglects penetration and standing-wave effects that are present under the true dynamic conditions. As main magnetic field strength B_0 increases, the MR frequency increases and the wavelength of the excitation B_1 field decreases. Hence, the approximation of a quasi-static excitation field, which is equivalent to assuming very long wavelengths, becomes less valid at higher field strengths.

The results of an analysis assuming static fields will at best match measurements made by placing a small pickup coil within the unloaded RF coil. Birdcage head coils have been measured in this manner to have in-plane uniformity with as little as 1% variation[1] when operating at 64 MHz (suitable for a standard 1.5-T magnet). However, since image intensity variations of 20% are often observed at this field strength, a model that predicts 1% variation is clearly unsatisfactory.

Initial attempts at dynamic modeling of MR excitation [3], [10] predicted that penetration effects would significantly degrade performance at frequencies above 30 MHz. As 64-MHz (1.5-T) machines have since become standard for clinical imaging, these predictions were clearly overly pessimistic. It has been suggested [2], [11] that this discrepancy is due to insulating structures in biological tissue that prevent large current loops from forming. However, calculations by Glover *et al.* [12] show substantially greater field penetration that has been confirmed by experiments with a cylindrical phantom at 64 MHz. A similar calculation by Zypman [13], taking into account the influence of the RF coil, arrived at the same solution for the field within a cylindrical phantom. Analysis of this kind predicts image intensity variations of 10%–20% in a head size structure, which is consistent with typically observed values. The magnitude of these variations suggest that electrodynamic interactions, rather than other effects such as deficiencies in the scanner, are the primary cause of intensity nonuniformity for 1.5-T machines.

A difficulty with analytic modeling is that closed form solutions are only available for simple geometries. Finite elements offer a more flexible approach to dynamic modeling of complicated structures. The problem of modeling the excitation field within the human head has been treated by

Manuscript received December 22, 1997; revised May 14, 1998. The Associate Editor responsible for coordinating the review of this paper and recommending its publication was Z.-P. Liang. *Asterisk indicates corresponding author.*

*J. G. Sled is with the McConnell Brain Imaging Centre, Montréal Neurological Institute and McGill University, 3801 University Street, Montréal, PQ, H3A 2B4, Canada (e-mail: jgsled@bic.mni.mcgill.ca).

G. B. Pike is with the McConnell Brain Imaging Centre, Montréal Neurological Institute and McGill University, Montréal, PQ, H3A 2B4, Canada.

Publisher Item Identifier S 0278-0062(98)08578-4.

[1]Field variation is given as the ratio of the range of field strengths to their mean computed over the volume of interest.

a number of authors [14]–[16]. Šimunić *et al.* [14] make the approximation of quasi-static conditions outside the head in modeling the fields generated by a linearly polarized saddle coil at 64 MHz. The results of these simulations have been validated *in vivo* using the dual-flip-angle technique described in [17]. Similar measurements [17] using a birdcage (circularly polarized) head coil did not detect a significant variation in B_1 field strength. These authors did not, however, use their results to predict the effect that these field variations have on image intensity variations.

In this paper, we investigate the extent to which electromagnetic interactions with the object account for the intensity nonuniformity observed in standard volumetric scans. To do so, we develop an analytic solution for the excitation field and reception sensitivity when imaging a cylinder with elliptic cross section. In the process, we clarify for the general case of a conducting object the relationship between the excitation field and the reception sensitivity of a coil. In addition, we investigate the hypothesis that an elliptically shaped object leads to a diagonal pattern of nonuniformity, even when excited by a circularly polarized coil. Our results are validated with phantom studies using both a standard imaging sequence and an *in vivo* B_1 field mapping technique.

II. Methods

A. Modeling the Excitation Field and Reception Sensitivity

While a variety of experimental and numerical approaches are available to investigate the effect of eccentric geometry on intensity nonuniformity, an analytic approach is used here for simplicity.

This treatment considers a long homogeneous dielectric cylinder with elliptic cross section excited by a circularly polarized field perpendicular to the cylinder axis. Only regions far from the ends of the cylinder are considered, interaction with the RF coils is neglected, and far from the cylinder the excitation field (B_1) is assumed to be uniform. The propagation of electric and magnetic fields in dielectric media is governed by the equations

$$\nabla^2 \mathbf{E} = \mu\epsilon \frac{\partial^2 \mathbf{E}}{\partial t^2} + \frac{\mu}{\rho}\frac{\partial \mathbf{E}}{\partial t} \tag{1}$$

$$\nabla \times \mathbf{E} = -\frac{\partial \mathbf{B}}{\partial t} \tag{2}$$

where $\mathbf{E}$ and $\mathbf{B}$ are the electric and magnetic fields, respectively, μ is the magnetic permeability, ϵ is the permittivity, and ρ is the resistivity of the media. The magnetic field B_1 is assumed to be oriented perpendicular to the cylinder axis while the electric field is oriented parallel. In addition, the solutions for the real vector fields $\mathbf{E}$ and $\mathbf{B}$ are assumed to vary sinusoidally in time at an angular frequency ω such that

$$\mathbf{E} = \mathrm{Re}\{E_z \hat{z} e^{j\omega t}\} \tag{3}$$

$$\mathbf{B} = \mathrm{Re}\{(B_x \hat{x} - jB_y \hat{y}) e^{j\omega t}\}. \tag{4}$$

Suppose the cross section of the ellipse is as shown in Fig. 1(a) with major and minor radii r_x and r_y, respectively.

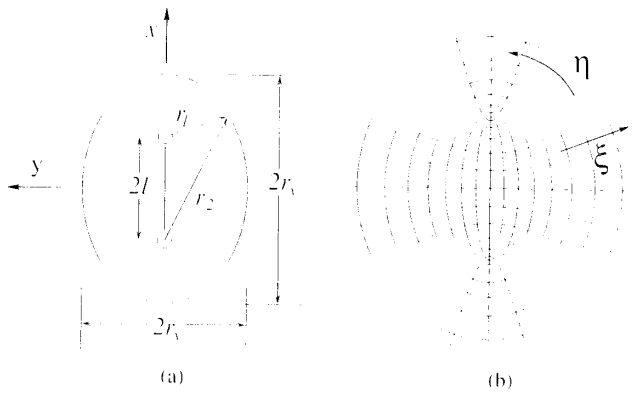

Fig. 1. (a) Elliptic cylinder geometry and (b) corresponding coordinate system.

Let $2l$ be the interfocal distance given by

$$l = \sqrt{r_x^2 - r_y^2}. \tag{5}$$

This geometry is simply expressed in a coordinate system formed from confocal ellipses and hyperbolas such that the radial and circumferential elliptic coordinates ξ and η are related to the Cartesian coordinates by

$$x = l \cosh \xi \cos \eta \tag{6}$$

$$y = l \sinh \xi \sin \eta \tag{7}$$

$$z = z. \tag{8}$$

Lines of constant ξ are ellipses, while lines of constant η are hyperbolas. Some examples are shown in Fig. 1(b).

This change of coordinates is one-to-one for $\xi > 0$ and $-\pi < \eta \leq \pi$ and can be inverted as follows

$$r_1 = \sqrt{(x - l)^2 + y^2} \tag{9}$$

$$r_2 = \sqrt{(x + l)^2 + y^2} \tag{10}$$

$$\xi = \cosh^{-1}\left(\frac{r_1 + r_2}{2l}\right) \tag{11}$$

$$\eta = \mathrm{sign}(y) \cos^{-1}\left(\frac{r_2 - r_1}{2l}\right). \tag{12}$$

Using (3) and (4), (1) and (2) can be rewritten in elliptic coordinates as

$$\frac{1}{\frac{1}{2}l^2(\cosh 2\xi - \cos 2\eta)}\left(\frac{\partial^2 E_z}{\partial \xi^2} + \frac{\partial^2 E_z}{\partial \eta^2}\right) + \frac{\partial^2 E_z}{\partial z^2} + k^2 E_z = 0 \tag{13}$$

$$\mathbf{B} = \frac{j}{\omega l \sqrt{\frac{1}{2}(\cosh 2\xi - \cos 2\eta)}}\left(\frac{\partial E_z}{\partial \eta}\hat{\xi} - \frac{\partial E_z}{\partial \xi}\hat{\eta}\right) \tag{14}$$

where $\hat{\xi}$ and $\hat{\eta}$ are unit vectors in the direction of the respective coordinates. k is the complex wave number given by $k = 2\pi/\lambda$, where

$$\lambda = \lambda_0 / \sqrt{\epsilon_r - j/\omega\epsilon_0\rho} \tag{15}$$

$$\lambda_0 = \frac{2\pi}{\omega\sqrt{\mu_0\epsilon_0}}. \tag{16}$$

λ is the reduced wavelength in the medium, λ_0 is the free space wavelength, ϵ_0 and μ_0 are the permittivity and permeability

of free space, and $\epsilon_r = \epsilon/\epsilon_0$ is the relative permittivity of the media. While in general ϵ_r is complex to account for losses due to bound electrons, these losses are typically small at the frequencies of interest for MRI. The magnetic permeability of biological materials differs little from that of free space [18] so we let $\mu = \mu_0$.

Since the cylinder is long, the z dependence of E_z can be ignored. Equation (13) is separable and admits solutions of the form $E_z = \Psi(\xi)\Phi(\eta)$ where Ψ and Φ are solutions of Mathieu's circumferential differential equation

$$\frac{d^2\Phi}{d\eta^2} + \left(c - \frac{h^2}{2}\cos 2\eta\right)\Phi = 0 \tag{17}$$

and Mathieu's radial differential equation

$$\frac{d^2\Psi}{d\xi^2} - \left(c - \frac{h^2}{2}\cosh 2\xi\right)\Psi = 0. \tag{18}$$

The two solutions Ψ and Φ are linked by c, referred to as the separation constant or Mathieu characteristic number (MCN). The constant $h = lk$.

For a given value of h there is an infinite set of discrete MCN's for which the solution to (17) is of period 2π. These solutions come in even and odd varieties referred to as $\mathrm{Se}_n(h, \eta)$ and $\mathrm{So}_n(h, \eta)$, respectively, and are analogous to the set of sines and cosines that are solutions to the problem of a cylinder with circular section. The corresponding solutions to the radial (18) are even and odd radial Mathieu functions of the first through fourth kind. Radial Mathieu functions of the first and second kind, evoked by an elliptic geometry, are analogous to Bessel functions, evoked by a circular geometry.

The Mathieu functions Se and So can be represented in terms of a sum of sines and cosines where the coefficients are related by a recurrence relation [19], [20]. The same set of coefficients is used to compute the corresponding radial Mathieu function expressed in terms of Bessel functions. The coefficients along with their corresponding MCN's are found using the nonlinear numerical optimization technique described in [20].

The problem of excitation by a circularly polarized coil is treated as excitation by two linearly polarized coils producing magnetic fields parallel to the x and y axes, respectively. The problem is simplified by assuming, as in [12] and [14], that the conditions outside the cylinder can be treated quasi-statically by taking k to be zero. This is valid provided the wavelength λ is much larger than the region of interest. At 64 MHz, λ is 4.7 m in air but only 53 cm in water; hence the quasi-static approximation is valid outside the cylinder but not inside for the cases considered in the following sections.[2]

Taking $h = 0$, (17) and (18) reduce to the Helmholtz equation and admit solutions of the form

$$\Psi_n(\xi) = e^{\pm n\xi} \tag{19}$$

$$\Phi_n(\eta) = \cos n\eta \tag{20}$$

$$\Phi_n(\eta) = \sin n\eta. \tag{21}$$

[2]The analysis of an elliptic cylinder is tractable without the assumption of quasi-static conditions outside the cylinder. However for the cases considered, the effect on the solution within the cylinder is negligible.

Treating the linearly polarized coil with axis oriented in the y direction first, the amplitude of the magnetic field far from the cylinder is required to be constant and oriented along y. The general solution for E_z satisfying this constraint is

$$E^y_z = j\omega h B_1\left(e^{\xi}\cos\eta + \sum_{m=1}^{\infty} p_m e^{-m\xi}\cos m\eta\right) \tag{22}$$

where B_1 is the magnitude of the magnetic field far from the cylinder and the notation E^y_z refers to the z component of the electric field external to the cylinder due to a y polarized coil.

Applying (14) to this solution leads to an expression for the radial and circumferential components of the magnetic field

$$B^y_{\xi} = B_1 G(\xi, \eta)\left(e^{\xi}\sin\eta + \sum_{m=1}^{\infty} m p_m e^{-m\xi}\sin m\eta\right) \tag{23}$$

$$B^y_{\eta} = B_1 G(\xi, \eta)\left(e^{\xi}\cos\eta - \sum_{m=1}^{\infty} m p_m e^{-m\xi}\cos m\eta\right) \tag{24}$$

where

$$G(\xi, \eta) = \frac{1}{\sqrt{\frac{1}{2}(\cosh 2\xi - \cos 2\eta)}}. \tag{25}$$

These solutions have the desired property that far from the cylinder the field is aligned with the y axis. That is

$$\lim_{\xi\to\infty} B^y_{\xi} = \lim_{\xi\to\infty} \frac{B_1 e^{\xi}\sin\eta}{\cosh\xi} = B_1\sin\eta \tag{26}$$

$$\lim_{\xi\to\infty} B^y_{\eta} = \lim_{\xi\to\infty} \frac{B_1 e^{\xi}\cos\eta}{\cosh\xi} = B_1\cos\eta. \tag{27}$$

The general solutions with corresponding symmetry for the interior of the cylinder are

$$E^y_z = j\omega h B_1 \sum_{n=0}^{\infty} q_n \mathrm{Je}_n(h, \xi)\mathrm{Se}_n(h, \eta) \tag{28}$$

$$B^y_{\xi} = B_1 G(\xi, \eta)\sum_{n=0}^{\infty} q_n \mathrm{Je}_n(h, \xi)\mathrm{Se}'_n(h, \eta) \tag{29}$$

$$B^y_{\eta} = B_1 G(\xi, \eta)\sum_{n=0}^{\infty} q_n \mathrm{Je}'_n(h, \xi)\mathrm{Se}_n(h, \eta) \tag{30}$$

where Je_n are even radial Mathieu functions of the first kind. The radial functions of the first kind have been chosen to satisfy the requirement that the magnetic field be continuous across the cut in the coordinate system corresponding to $\xi = 0$.

It should be noted that, unlike the case of a cylinder with circular section, there is not a one-to-one correspondence between the individual terms of the interior solution and the exterior solution. The problem of matching the interior solutions at the boundary is overcome by truncating the series solutions and solving for the coefficients numerically. Similarly, the series expressions for the individual Mathieu functions are truncated to make numerical evaluation tractable. In practice, the coefficients in these series drop off extremely rapidly and the series can be accurately approximated by a

small number of terms. Details of this calculation are given in the Appendix.

The solution for the linearly polarized coil oriented along x is similar. The expressions for the electric and magnetic fields are

$$E'_{zx} = -j\omega hB_1\left(e^{\xi}\sin\eta + \sum_{m=1}^{\infty} p_m e^{-m\xi}\sin m\eta\right) \quad (31)$$

$$B'_{\xi x} = B_1 G(\xi,\eta)\left(e^{\xi}\cos\eta + \sum_{m=1}^{\infty} m p_m e^{-m\xi}\cos m\eta\right) \quad (32)$$

$$B'_{\eta x} = -B_1 G(\xi,\eta)\left(e^{\xi}\sin\eta - \sum_{m=1}^{\infty} m p_m e^{-m\xi}\sin m\eta\right) \quad (33)$$

$$E'_{zx} = -j\omega hB_1\sum_{n=0}^{\infty} q_n \mathrm{Jo}_n(h,\xi)\mathrm{So}_n(h,\eta) \quad (34)$$

$$B'_{\xi x} = B_1 G(\xi,\eta)\sum_{n=0}^{\infty} q_n \mathrm{Jo}_n(h,\xi)\mathrm{So}'_n(h,\eta) \quad (35)$$

$$B'_{\eta x} = -B_1 G(\xi,\eta)\sum_{n=0}^{\infty} q_n \mathrm{Jo}'_n(h,\xi)\mathrm{So}_n(h,\eta) \quad (36)$$

and the coefficients p_m and q_m can be solved for in an analogous manner. It should be noted that the MCN's for the odd Mathieu functions are not the same as those of the even functions. As a result, the field patterns generated by the two orthogonal coils are not related in a simple way.

Following the derivation in [12] and [21], the individual linearly polarized fields can be decomposed into two counter rotating fields, only one of which causes MR excitation. That is

$$\mathbf{B} = 1/2(B_\xi + jB_\eta)e^{j\alpha(\xi,\eta)}\mathbf{a}^+ + 1/2(B^*_\xi + jB^*_\eta)e^{j\alpha(\xi,\eta)}\mathbf{a}^- \quad (37)$$

where * denotes complex conjugate and $\mathbf{a}^\pm$ represent vectors rotating at angular frequency ω in the clockwise ($-$) and counterclockwise ($+$) directions. $\alpha(\xi,\eta)$ is the angle of rotation between the (ξ,η) and (x,y) coordinate systems, where

$$e^{j\alpha(\xi,\eta)} = \frac{\sinh\xi\cos\eta + j\cosh\xi\sin\eta}{\sqrt{\frac{1}{2}(\cosh 2\xi - \cos 2\eta)}}. \quad (38)$$

The convention that the $\mathbf{a}^+$ component produces MR excitation is followed here.

A so-called circularly polarized excitation field is created by driving the linear coils 90° out of phase such that the two signal producing fields add constructively. However, in general the field produced by a linearly polarized coil will vary in magnitude and direction within the object such that the combined field from the two coils can have arbitrary elliptic polarization. This elliptically polarized field can be decomposed into a ($+$) rotating field which causes the excitation and a typically weaker ($-$) rotating field that does not [21]. The orientation of this ($+$) rotating field with respect to the driving field can be interpreted as a phase shift, which we refer to as a geometric phase shift.

In general, the individual field components will be complex to reflect the phase delays caused by currents induced in the object. Geometric and inductive phase shifts combine to determine the local phase of the excitation field within the object as follows:

$$B^+ = 1/2(B_{\xi x} + jB_{\eta x} - jB_{\xi y} + B_{\eta y})e^{j\alpha(\xi,\eta)}. \quad (39)$$

Note that since the ξ and η directions are orthogonal, the field components B_ξ and B_η can be interpreted as being 90° out of phase. While this derivation is based on two linearly polarized coils aligned with the x and y axes, (39) is general for any combination of coils producing a circularly polarized field. Hence, it can used to predict the field pattern of a birdcage coil or a pair of linearly polarized coils not aligned with the x and y axes.

The same solutions for the field components apply when orthogonal coils are used for reception. However, the geometric phase shifts caused by reception cancel with those of the excitation field [1] whereas the phase shifts due to induced currents accumulate. Hence, the reception sensitivity is given by

$$R^+ = R_0/2(B_{\xi x} - jB_{\eta x} + jB_{\xi y} + B_{\eta y})e^{-j\alpha(\xi,\eta)} \quad (40)$$

where R_0 is a scale factor reflecting the sensitivity of the coil.

B. Simulating Spin Echo Images

Images produced by a spin-echo sequence are simulated using the excitation fields and reception sensitivity derived in the previous section. The signal measured for a spin-echo pulse sequence, as shown in [12], is given by

$$S(\xi,\eta) = R^+(\xi,\eta)S_{SE}(\xi,\eta) \quad (41)$$

$$S_{SE}(\xi,\eta) = \sin^3\left(\frac{\pi}{2}\frac{|B^+|}{B_m}\right)\exp\left(j\arg\left(B^+\right)\right) \quad (42)$$

where S_{SE} is the emitted signal, S is the measured signal, and B_m is the nominal field strength needed to produce a 90° flip angle. This derivation neglects relaxation and assumes complete recovery of the magnetization between repetitions. It also assumes that the pulses are nonselective or so-called hard pulses.

We refine (42) by taking into account the variations in slice profile caused by variations in excitation field strength. This is done by simulating frequency selective RF pulses using the Bloch equations [22] across the range of frequencies corresponding to a slice. The strength of the measured signal is proportional to the integral of the resulting slice profile. This simulation was carried out for a range of field strengths to determine the variations in signal intensity with field strength. A comparison of S_{SE} for selective and nonselective pulses is shown in Fig. 2. Equation (42) is a good approximation for selective pulse except at the high B_1 field strengths corresponding to severe intensity nonuniformity.

In simulating a spin-echo image, the factor B_m is arbitrary. Typically, an MRI machine will calibrate B_m for each subject to maximize signal intensity.

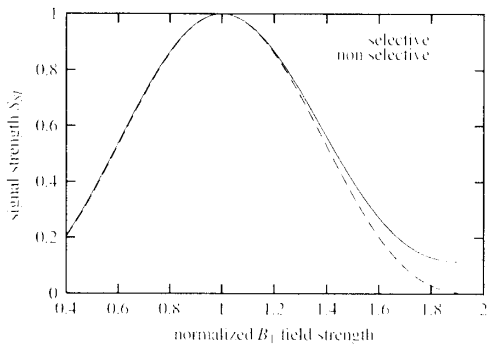

Fig. 2. Signal intensity versus B_1 field strength for selective and nonselective pulses. The results for selective pulses are based on simulation of a standard spin-echo sequence for a 1.5-T Siemens Vision MRI machine, which uses numerically optimized pulse profiles.

C. Phantom Studies

We constructed two plastic cylindrical containers with elliptic and circular cross sections, respectively, to validate our model of intensity nonuniformity. The circular cylinder has an inside diameter of 17.5 cm, while the elliptic cylinder has major and minor diameters of 20 and 15 cm. Each cylinder was filled with various concentrations of NaCl solutions made from deionized water.

The conductivity and permittivity of each solution was computed based on the concentration of NaCl using data from [23]. The quantities of NaCl were 1.38, 2.83, and 58.2 g/L, or roughly 24, 48, and 100 mM, producing resistivities of 4.0, 2.0, and 1.0 Ωm, respectively. These resistivities span the range typical of biological tissues [3] at frequencies around 64 MHz. At this frequency, the relative permittivity of water is essentially unchanged from its dc value of $\epsilon_r = 80$, which is comparable to that of brain [14] at 64 MHz. In addition to NaCl, a small quantity of $MnCl_2$ was added to each solution to bring its concentration to 97 μM and reduce T_1 relaxation times to approximately 910 ms. Experiments using long repetition times (TR = 30 s) showed no measurable change in intensity nonuniformity after addition of $MnCl_2$.

The cylinders were designed to have a length, 40 cm, such that for transverse measurements near the center, the field patterns are essentially the same as for a cylinder of infinite length. This is true if the cylinder is longer than twice the skin depth for the medium [12] and the region being considered is close enough to the center to avoid variations caused by dielectric resonance along the cylinder's length. In practice, the former was found to be the more restrictive criteria. The skin depth is given by $\delta = \sqrt{2\rho/\mu\omega}$ which corresponds to between 6.3 and 12.6 cm for the given solutions.

For the experiments, the cylinders were aligned axially with the isocenter of the body coil of a 1.5-T Siemens Vision MRI scanner and scanned transversally using a B_1 field mapping sequence [24] as well as a standard spin-echo sequence. All images are acquired at 2-mm in-plane resolution with 6-mm-thick slices. The spin-echo sequence (TR/TE = 8 s/11 ms) had sufficiently short TE and long TR that relaxation can be neglected. The field mapping sequence is a stimulated echo technique $(90^\circ - \tau_e/2 - 90^\circ - \tau_1 - \alpha - \tau_2 - 90^\circ - \tau_e/2 - acq.$ where $\tau_e/\tau_1/\tau_2/TR = 36$ ms/60 ms/8 ms/1 s) which yields a series of images whose intensities are related by

$$S_i = a \cos b\alpha_i. \tag{43}$$

The parameters a and b are computed at each voxel by a nonlinear least squares fit to the flip angles α_i and complex image values S_i. Images were acquired at $\alpha = 0^\circ, 40^\circ, \cdots, 100^\circ$. The resulting parameter map b is proportional to the excitation field strength, while the parameter map a is roughly proportional to spin density.

D. Comparing Fields and Images

The experimental data admits two types of comparisons with the theoretical model: a direct comparison of the measured excitation field with that predicted, and a comparison of the measured spin-echo image with that simulated from the predicted excitation field and reception sensitivity. Before any comparisons were made all of the measured data was first automatically registered [25], [26] with the spin density map of the corresponding simulated image by linear transformation. The effect of nonuniformity on the registration was minimized by matching smoothed gradient images rather than the images themselves. The measured field maps, which lack well-defined object boundaries, were registered indirectly by registering the a parameter map to the simulation then applying the same transformation to the field map.

For quantitative comparison a common mask was defined for each pair of images within which differences could be calculated. The mask was defined by automatically thresholding each image based on its histogram [27], taking the intersection of the two masks, and eroding it by 2 mm. The standard of comparison we use is the root mean square (rms) difference between two images computed within the common mask and expressed as a percentage of the mean intensity in the simulated image.

In the case of comparisons involving simulated spin-echo images there is the factor B_m which remains uncertain. Since this factor is not readily determined for an experimental measurement, a single factor B_m is chosen to minimize the rms difference between the simulated and measured image.

III. Results

A. Variations in Field Strength

The resulting pattern of variations in image intensity can be understood by considering the simpler pattern of variations that appear in the excitation field and reception sensitivity. These in turn can be better understood by decomposing the circularly polarized field into two orthogonal linear fields acting in quadrature. Consider the field patterns arising in the elliptic and circular cylinders described earlier. We illustrate in Fig. 3 the case of a homogeneous medium having the properties: $\mu = \mu_0$, $\epsilon_r = 80$, and $\rho = 2$ Ωm. Fig. 3(a) and (b) shows the two geometries, while Fig. 3(c) and (d) shows the magnitude of the rotating excitation field B^+ when

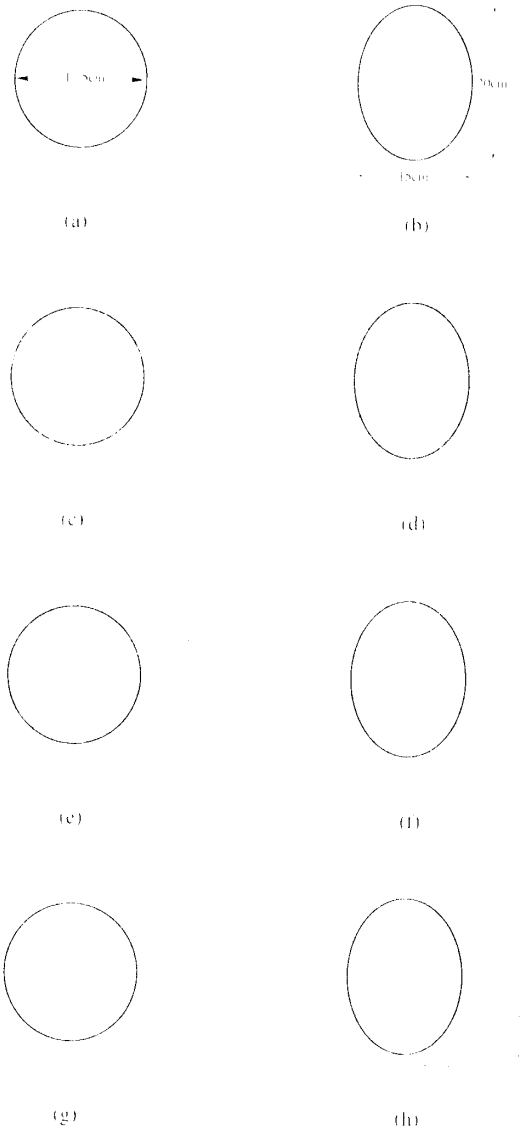

Fig. 3. Magnitude contours of B^+, the rotating component of the magnetic field resulting in excitation. Each field is normalized to have a mean of 1.0 and contours are drawn at 5% intervals. See text for explanation.

driven by a coil whose nominal field is oriented parallel to the minor axis of the ellipse. This linearly polarized coil produces the expected "quadrapole" pattern with brighter intensities to the top-right and bottom left. The orientation of this diagonal pattern depends on the properties of the media as well as the eccentricity of the cylinder section.

The corresponding magnitude contours for a coil producing a field oriented along the major axis of the ellipse are shown for the two geometries in Fig. 3(e) and (f). In the case of the circular section, the field pattern is rotated by 90°, while in the case of the elliptic section the field pattern is rotated but is also more uniform. Each contour in these plots is a five percent increment in field strength. Combining the two linearly polarized cases, taking into account the 90° phase difference, produces the field patterns shown in Fig. 3(g) and (h). In the case of the circular section, the low-intensity regions of one coil cancel with the high-intensity regions of the other

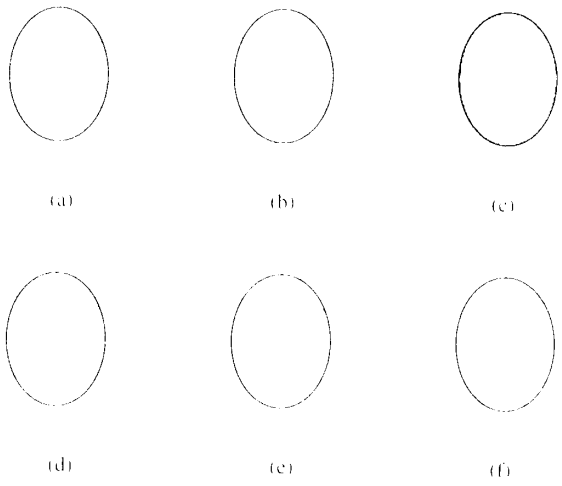

Fig. 4. Simulated spin-echo images with nominal 90 and 180° flip angles. Contours are at 5% of mean intensity. (a) and (d): magnitude and phase, respectively, of the excitation field B^+. (b) and (e): magnitude and phase of the reception sensitivity B^-. (c) and (f): magnitude and phase of the resulting spin-echo image.

to produce a field that is axially symmetric and relatively uniform. In the case of the elliptic section these regions do not fully cancel and some of the diagonal pattern remains. It is this lack of cancellation that accounts for the diagonal pattern seen in MR images of eccentric objects. It should be noted that since the fields are complex, combining the fields is not the same as adding the two magnitude images. It is also of note that despite having similar volume to the circular cylinder, the range of variation in field magnitude is greater in the elliptic cylinder.

B. Simulated Spin Echo Images

Once the excitation field and reception sensitivity have been evaluated they can be used to simulate an imaging sequence. A simulated spin-echo image for an elliptic geometry having the same properties as for Fig. 3 is shown in Fig. 4. Also shown are the corresponding excitation field and reception sensitivity.

It should be noted that the pattern of nonuniformity in the spin-echo image resembles neither the excitation field nor the reception sensitivity. This is caused by the apparent reversal of the excitation field to produce the sensitivity map. However, close inspection of the phase images for the two cases reveals that the excitation field and reception sensitivity maps differ by more than a reversal. In particular the geometric phase in the two cases is opposite while the inductive phase lag, dominant in this medium, remains unchanged.

Due to the symmetry of the elliptic shape, the magnitude of the excitation and reception sensitivity maps differ only by a reversal of the y axis. However, the resulting spin-echo image is not symmetric as reception sensitivity makes a stronger contribution to image nonuniformity than does excitation field variation.

C. Pulse Sequence Sensitivity

To explain the relative contribution of excitation field and reception sensitivity variation to image nonuniformity, con-

sider a first-order perturbation on the measured signal $S = S_m + \delta S$ caused by a perturbation $B = B_m + \delta B$ to the B_1 field strength and receiver sensitivity. Substituting these expressions into (41) and treating the signal as real leads to an expression for the sensitivity of a spin-echo imaging sequence

$$\frac{S_m + \delta S}{S_m} = \frac{B_m + \delta B}{B_m} \sin^3\left(\frac{\pi}{2}\frac{B_m + \delta B}{B_m}\right)$$

$$1 + \frac{\delta S}{S_m} = \left(1 + \frac{\delta B}{B_m}\right)\cos^3\left(\frac{\pi}{2}\frac{\delta B}{B_m}\right)$$

$$1 + \frac{\delta S}{S_m} = \underbrace{\left(1 + \frac{\delta B}{B_m}\right)}_{\text{reception}} \underbrace{\left(1 - \frac{3\pi^2}{8}\left(\frac{\delta B}{B_m}\right)^2 + O\left(\frac{\delta B}{B_m}\right)^3\right)}_{\text{excitation}} \tag{44}$$

$$\frac{\delta S}{S_m} = \frac{\delta B}{B_m} - \frac{3\pi^2}{8}\left(\frac{\delta B}{B_m}\right)^2 + O\left(\frac{\delta B}{B_m}\right)^3. \tag{45}$$

This expression represents the fractional change in measured signal caused by a given fractional variation in field magnitude and reception sensitivity.

It should be noted from (44) that, while the dependence on reception sensitivity is first order, the dependence on excitation uniformity is second order. Hence, the sequence is less sensitive to variations in the excitation field than variations in reception sensitivity.

The comparable expression for a gradient-echo sequence which only involves a single 90° RF excitation and neglects relaxation effects is

$$\frac{\delta S}{S_m} \approx \frac{\delta B}{B_m} - \frac{\pi^2}{8}\left(\frac{\delta B}{B_m}\right)^2 + O\left(\frac{\delta B}{B_m}\right)^3. \tag{46}$$

While the sensitivities of 90° gradient-echo and 90°–180° spin-echo sequences differ only in the second-order terms, it should be noted that gradient-echo sequences are commonly used with lower flip angles. For example, the expression for the sensitivity of a gradient-echo sequence with a 45° flip angle is given by

$$\frac{\delta S}{S_m} \approx \left(1 + \frac{\pi}{4}\right)\frac{\delta B}{B_m} + \frac{\pi}{4}\left(1 - \frac{\pi}{8}\right)\left(\frac{\delta B}{B_m}\right)^2 + O\left(\frac{\delta B}{B_m}\right)^3 \tag{47}$$

which means that the sequence is 78% more sensitive to field variations than the other two.

D. Influence of Media Properties

In continuing to investigate the character of intensity nonuniformity, consider the effect that the properties of the media have on the shape of the nonuniformity observed. Simulated images for a number of combinations of ϵ_r and ρ are shown in Fig. 5. Increasing the resistivity of the media from its nominal value of 2–20 Ωm, as shown in Fig. 5(a), decreases the image uniformity by enhancing the signal in the center of the cylinder. This cup shaped intensity variation is normally attributed to standing-wave effects. Decreasing the resistivity to 0.5 Ωm, as shown in 5(b), reverses the cup shaped variation and produces the strongest intensity in a rim at the edge. The reduced intensity at the center is often described as an RF penetration effect, caused by induced currents. Reducing the relative permittivity to 40, as in 5(c), produces the most uniform image. This is consistent with making the properties of the media more like the surrounding space. Increasing the relative permittivity to 160, a value larger than typically found in biological tissue, produces the wave-like nonuniformity pattern shown in 5(d). This behavior is consistent with the reduced wavelength being smaller than the dimensions of the cylinder. To some extent, RF penetration and standing-wave effects are complementary in that one enhances the intensity near the center while the other diminishes it. The properties of biological tissue are such that there is cancellation between the two effects, perhaps accounting for the better than predicted uniformity of 1.5-T MRI images.

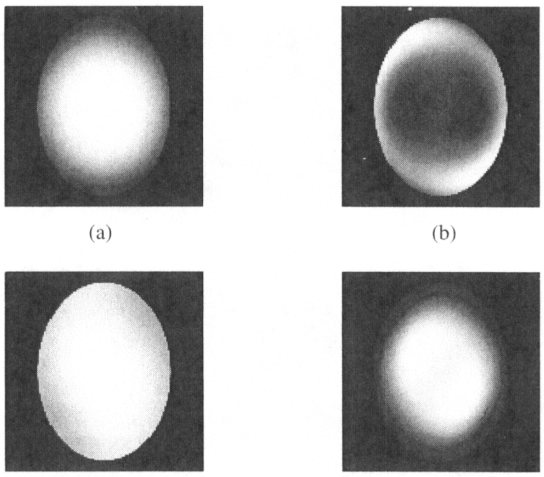

Fig. 5. Simulated spin-echo images of a cylinder with elliptic section for various values of ϵ_r and ρ. (a) $\rho = 20$ Ωm and $\epsilon_r = 80$, (b) $\rho = 0.5$ Ωm and $\epsilon_r = 80$, (c) $\rho = 2$ Ωm and $\epsilon_r = 40$, and (d) $\rho = 2$ Ωm and $\epsilon_r = 160$.

E. Comparison with Phantom Studies

Validation of our model for intensity nonuniformity is provided by comparing the predicted results with experimental results obtained from flood phantoms. The excitation field patterns were compared with direct measurements of the excitation field using the pulse sequence described previously. As the reception sensitivity cannot be measured directly, we evaluated our predictions indirectly through their impact on spin-echo images.

Fig. 6 shows the excitation fields measured in the elliptic cylinder for each of the three NaCl solutions. Also shown are the predicted field patterns and the differences between the measured and predicted results. The prediction of a diagonal pattern of nonuniformity is confirmed by these experiments. When the gray scale of the difference image is expanded, it reveals minor and largely random differences between the measured and predicted images. The accuracy of the results for the circular cylinder is essentially the same.

The accuracy of the model at predicting the measured images was quantified by computing the rms difference between the two. These results are given for the two geometries and three NaCl solutions in Table I along with the standard

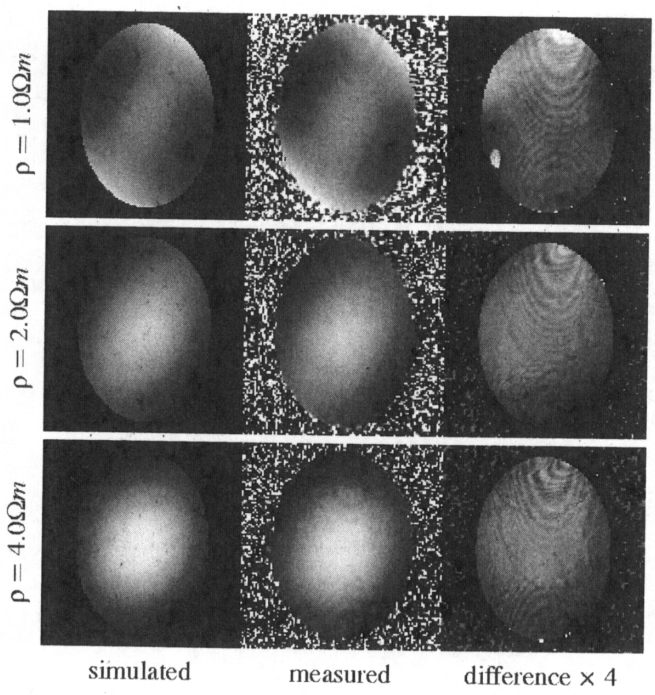

Fig. 6. Comparison of predicted and measured excitation fields B^+ in an elliptic phantom for three levels of resistivity. The normalized intensity scale for each image is 0.8–1.2, except for the difference images which are −0.05–0.05.

TABLE I
SUMMARY OF COMPARISONS BETWEEN SIMULATED AND MEASURED EXCITATION FIELDS. ALL VALUES ARE EXPRESSED AS A PERCENTAGE OF THE MEAN INTENSITY IN THE SIMULATED IMAGE

	circular phantom		
	1.0Ωm	2.0Ωm	4.0Ωm
SD of simulated field	2.02%	6.05%	7.43%
SD of measured field	2.31%	5.17%	6.28%
rms difference	1.37%	1.37%	1.61%
	elliptic phantom		
	1.0Ωm	2.0Ωm	4.0Ωm
SD of simulated field	5.40%	6.59%	7.42%
SD of measured field	5.49%	5.98%	6.84%
rms difference	1.31%	1.21%	0.99%

deviation (SD) of the intensity in each image. Table I shows that the SD, a measure of the severity of the nonuniformity, increases with resistivity while the absolute accuracy of the model remains constant.

Fig. 7 shows the measured and predicted spin-echo images for the two geometries and three solutions. The pattern of variations in these images is more complicated and the variations are more severe due to the contribution of the reception sensitivity. Note that the orientation of the diagonal pattern in the elliptic case is reversed with respect to the excitation field map.

The accuracy of the predicted spin-echo images, quantified in terms of image SD and the rms difference between measured and predicted results, is given in Table II. The accuracy of these results is slightly poorer than for the excitation fields; however, the nonuniformity is also more severe. Hence, in relative terms the accuracy of the predicted spin-echo images

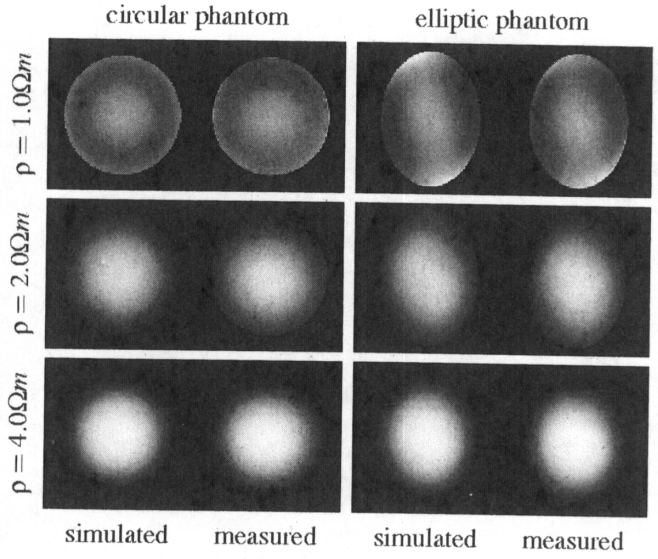

Fig. 7. Comparison of predicted and measured spin-echo images for each level of resistivity. The normalized intensity scale for each image is 0.8–1.2.

TABLE II
SUMMARY OF COMPARISONS BETWEEN SIMULATED AND MEASURED SPIN ECHO IMAGES. ALL VALUES ARE EXPRESSED AS A PERCENTAGE OF THE MEAN INTENSITY IN THE SIMULATED IMAGE

	circular phantom		
	1.0Ωm	2.0Ωm	4.0Ωm
SD of simulated image	3.09%	7.65%	10.04%
SD of measured image	3.19%	7.57%	10.39%
rms difference	1.83%	1.65%	1.81%
	elliptic phantom		
	1.0Ωm	2.0Ωm	4.0Ωm
SD of simulated image	4.68%	7.98%	10.85%
SD of measured image	5.22%	8.04%	11.14%
rms difference	2.25%	1.83%	2.01%

is comparable to that for the excitation fields. As before, the absolute accuracy of the results remains unchanged as the resistivity increases.

F. Field Variations in the Human Head

As a final result, a transverse image of the excitation field was acquired for a human subject using a circularly polarized body coil and the B_1 field mapping sequence described in Section II-C. This image and a corresponding spin-echo image (TE/TR = 14 ms/500 ms) are shown in Fig. 8. The standard deviation of field intensity computed within a hand drawn brain mask is 4.0%, comparable to that measured in the phantoms. Also note that, while less pronounced, the field map shows a diagonal pattern of variation suggestive of that observed in the elliptic phantom.

IV. DISCUSSION

Through an electrodynamic treatment of the MR excitation and reception process, it has been shown that an elliptic geometry imaged using circularly polarized coils produces a diagonal intensity nonuniformity pattern qualitatively similar to the quadrapole artifact observed with linearly polarized

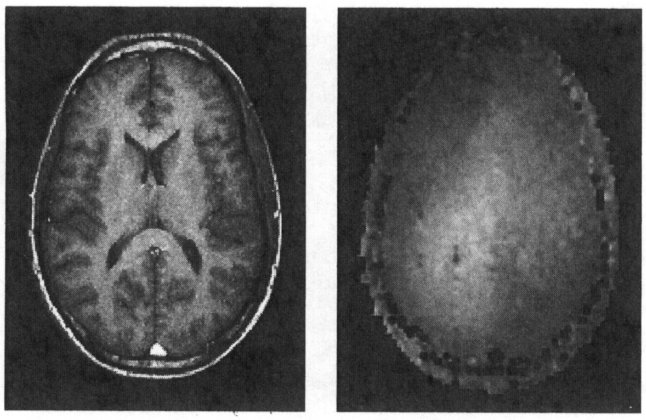

(a) (b)

Fig. 8. (a) A transverse spin-echo image and (b) corresponding excitation field map for a human subject. The normalized intensity scale for the field map is 0.8–1.2.

coils. Although, one would expect the circularly symmetric pattern seen for circular objects to generalize to an elliptically symmetric pattern for elliptic objects, decomposition of the circularly polarized field into two linearly polarized fields acting in quadrature reveals a difference between the two cases. In particular, in the circular case the two linear fields are mirror images of one another, whereas in the elliptic case the two linear fields interact differently with the media leading to asymmetric intensity variations that do not cancel in the combined field. Such asymmetry might be incorrectly attributed to right–left hemisphere differences in a sensitive statistical analysis of neurological scans. In addition, an elliptic geometry excited by a circularly polarized field is not equivalent to a circular geometry excited by an elliptically polarized field. The impact that this asymmetry has on the intensity variations observed in typical images is further complicated by the asymmetry between the excitation field and reception sensitivity for conductive objects.

Inspection of the experimental results for the elliptic case would suggest that the reception sensitivity is the mirror image of the excitation field pattern. However, the theoretical results show a more subtle relationship. In particular, for conductive objects there is a distinction between the phase delays associated with induced currents and those inherent in imaging the object in the absence of conductivity. The cancellation of the latter between excitation and reception but not the former leads to the nonuniformity pattern in the spin-echo image being more complicated than either the excitation or receptions fields. An implication of this result is that for arbitrarily shaped conductive objects, measurement of the complex excitation field is not sufficient to predict the pattern of variations in the resulting image.

While the difficulty of measuring both the excitation field and reception sensitivity has motivated the development of a variety of data-driven techniques for correcting for intensity nonuniformity [4]–[8], none of these methods accurately account for the underlying physics. The fact that a diagonal pattern of nonuniformity appeared in both the scans of an elliptic phantom and a human head, suggests that one may predict the pattern of variations without a detailed model of the particular subject. Such an approach to correcting for nonuniformity would require numerical techniques to properly treat the 3D problem and to account for the influence of the smaller coils typically used in head imaging.

The good agreement between the predicted and measured results suggests that most of the nonuniformity is accounted for by the electromagnetic interactions described in the model. This agreement is achieved in spite of making no explicit assumptions of a coil producing the fields. While this is reasonable for a head-sized object in a body coil, one can expect that smaller coils such as a head coil would produce some variations caused by their interaction with the object. However, in either case electromagnetic interaction with the object is the primary cause of intensity nonuniformity and further improvements in the uniformity of the unloaded coil will yield little improvement in uniformity.

V. Conclusions

Intensity nonuniformity is largely caused by interaction of the subject with the excitation field and reception sensitivity and will be present irrespective of the uniformity of the field produced by the unloaded coil. While the magnitude of the artifact depends on the pulse sequence, its shape has been shown to depend on geometry as well the resistive and permittive properties of the subject. In particular, an elliptic geometry is found to produce a diagonal pattern of nonuniformity. Despite the similarity between this artifact and the quadrapole artifact seen with linearly polarized coils, an elliptic geometry driven by a circularly polarized field is not equivalent to a circular geometry driven by an elliptically polarized field. While this fact prevents simple compensation for an elliptic geometry, the results of our analysis can be used as a guide in developing methods to correct for this artifact.

Appendix
Computing an Approximate Solution

Coefficients p_m from (22) and q_n from (28) are found by matching the solutions for the interior and exterior of the cylinder as follows. Suppose that $\mathrm{Se}_n(h, \eta)$ and $\mathrm{Se}'_n(h, \eta)$ are approximated as

$$\mathrm{Se}_n(h, \eta) = \sum_{m=0}^{M} r_{mn} \cos m\eta \tag{48}$$

$$\mathrm{Se}'_n(h, \eta) = -\sum_{m=0}^{M} m r_{mn} \sin m\eta \tag{49}$$

for $n = 0, \cdots, N$. Then the coefficients r_{mn} can be taken as the terms of a matrix R. Similarly, if the cylinder boundary is taken to be $\xi = \xi_0$ then the following matrices are defined as:

$$Q = [q_0\, q_1\, \cdots\, q_N]^T \tag{50}$$

$$P = [0\, p_1\, \cdots\, p_M]^T \tag{51}$$

$$J = \mathrm{diag}\big(\mathrm{Je}_0(h, \xi_0),\, \mathrm{Je}_1(h, \xi_0),\, \cdots,\, \mathrm{Je}_N(h, \xi_0)\big) \tag{52}$$

$$J' = \mathrm{diag}\big(\mathrm{Je}'_0(h, \xi_0),\, \mathrm{Je}'_1(h, \xi_0),\, \cdots,\, \mathrm{Je}'_N(h, \xi_0)\big) \tag{53}$$

$$X = \mathrm{diag}(0,\, 1,\, 2,\, \cdots,\, M) \tag{54}$$

$$Y = \mathrm{diag}(0,\, e^{-\xi_0},\, 2e^{-2\xi_0},\, \cdots,\, Me^{-M\xi_0}) \tag{55}$$

$$Z = \left[0\, e^{-\xi_0}\, 0\, 0\, \cdots\, 0\right]^T \tag{56}$$

where the notation diag$(\cdot)$ refers to a matrix with the given elements along its diagonal.

Equating the internal and external fields at the cylinder boundary leads to the following matrix equations:

$$B'_{\xi_0}(\xi_0, \eta) = B^e_{\xi_0}(\xi_0, \eta) \Rightarrow XRJQ = Z + YP \quad (57)$$

$$B'_{\eta_0}(\xi_0, \eta) = B^e_{\eta_0}(\xi_0, \eta) \Rightarrow RJ'Q = Z - YP \quad (58)$$

which can be solved for the coefficients p_m and q_m as

$$Q = 2(RJ' + XRJ)^{-1}Z \quad (59)$$

$$P = Y^{-1}(XRJQ - Z). \quad (60)$$

REFERENCES

[1] E. R. McVeigh, M. J. Bronskill, and R. M. Henkelman, "Phase and sensitivity of receiver coils in magnetic resonance imaging," *Med. Phys.*, vol. 13, pp. 806–814, Nov./Dec. 1986.

[2] A. Simmons, P. S. Tofts, G. J. Barker, and S. R. Arridge, "Sources of intensity nonuniformity in spin-echo images," *Magn. Reson. Med.*, vol. 32, pp. 121–128, 1994.

[3] P. A. Bottomley and E. R. Andrew, "RF magnetic field penetration, phase shift and power dissipation in biological tissue: Implications for NMR imaging," *Phys. Med., Biology*, vol. 23, pp. 630–643, July 1978.

[4] B. M. Dawant, A. P. Zijdenbos, and R. A. Margolin, "Correction of intensity variations in MR images for computer-aided tissue classification," *IEEE Trans. Med. Imag.*, vol. 12, pp. 770–781, Dec. 1993.

[5] C. R. Meyer, P. H. Bland, and J. Pipe, "Retrospective correction of intensity inhomogeneities in MRI," *IEEE Trans. Med. Imag.*, vol. 14, pp. 36–41, Mar. 1995.

[6] P. A. Narayana, W. W. Brey, M. V. Kulkarni, and C. L. Sievenpiper, "Compensation for surface coil sensitivity variation in magnetic resonance imaging," *Magn. Reson. Imag.*, vol. 6, no. 3, pp. 271–274, 1988.

[7] W. M. Wells, III, W. E. L. Grimson, R. Kikinis, and F. A. Jolesz, "Adaptive segmentation of MRI data," *IEEE Trans. Med. Imag.*, vol. 15, pp. 429–442, Oct. 1996.

[8] J. G. Sled, A. P. Zijdenbos, and A. C. Evans, "A nonparametric method for automatic correction of intensity nonuniformity in MRI data," *IEEE Trans. Med. Imag.*, vol. 17, pp. 87–97, Feb. 1998.

[9] S. E. Moyher, D. B. Vigneron, and S. J. Nelson, "Surface coil MR imaging of the human brain with an analytic reception profile correction," *J. Magn. Reson. Imag.*, vol. 5, pp. 139–144, Mar./Apr. 1995.

[10] P. Mansfield and P. G. Morris, *NMR Imaging in Biomedicine*, Advances in Magnetic Resonance, Suppl. 2. New York: Academic, 1982, pp. 181–191.

[11] P. Roschmann, "Radiofrequency penetration and absorption in the human body: Limitations to high-field whole-body nuclear magnetic resonance imaging," *Med. Phys.*, vol. 14, pp. 922–931, Nov.–Dec. 1987.

[12] G. O. Glover, C. E. Hayes, N. J. Pelc, W. A. Edelstein, O. M. Mueller, H. R. Hart, C. J. Hardy, M. O'Donnel, and W. D. Barber, "Comparison of linear and circular polarization for magnetic resonance imaging," *J. Magn. Reson.*, vol. 64, pp. 255–270, 1985.

[13] E. R. Zypman, "MRI electromagnetic field penetration in cylindrical objects," *Comput. Biol., Med.*, vol. 26, pp. 161–175, Mar. 1996.

[14] D. Simunic, P. Wach, W. Renhart, and R. Stollberger, "Spatial distribution of high-frequency electromagnetic energy in human head during MRI: Numerical results and measurements," *IEEE Trans. Biomed. Eng.*, vol. 43, pp. 88–94, Jan 1996.

[15] J. T. Vaughan, H. P. Hetherington, J. O. Otu, J. W. Pan, and G. M. Pohost, "High frequency volume coils for clinical NMR imaging and spectroscopy," *Magn. Reson. Med.*, vol. 32, pp. 206–218, Aug. 1994.

[16] J. Jin and J. Chen, "On the SAR and field inhomogeneity of birdcage coils loaded with the human head," *Magn. Reson. Med.*, vol. 38, pp. 953–963, Dec. 1997.

[17] R. Stollberger and P. Wach, "Imaging of the active B1 field in vivo," *Magnetic Resonance in Medicine*, vol. 35, pp. 246–251, 1996.

[18] *CRC Handbook of Chemistry and Physics*, 55th ed. Boca Raton, FL: CRC, 1974–75, pp. E126–E134.

[19] *Handbook of Mathematical Functions*, 9th ed., M. Abramowitz and I. A. Stegun, Eds. New York: Dover, 1972.

[20] F. A. Alhargan, "Complete method for the computations of Mathieu characteristic numbers of integer orders," *SIAM Rev.*, vol. 38, pp. 239–255, June 1996.

[21] P. S. Tofts, "Standing waves in uniform water phantoms," *J. Magn. Reson., B*, vol. 104, pp. 143–147, 1994.

[22] F. Bloch, W. Hanson, and M. Packard, "Nuclear induction," *Phys. Rev.*, vol. 69, p. 127, Feb. 1946.

[23] P. S. Neelakanta, *Handbook of Electromagnetic Materials: Monolithic and Composite Versions and Their Applications*. Boca Raton, FL: CRC, 1995, pp. 577–584.

[24] S. Topp, E. Adalsteinsson, and D. M. Spielman, "Fast multislice B_1-mapping," in *Proc. Int. Society for Magnetic Resonance in Medicine, Fifth Scientific Meeting and Exhibition* 1997, vol. 1, p. 281.

[25] D. L. Collins, P. Neelin, T. M. Peters, and A. C. Evans, "Automatic 3-D intersubject registration of MR volumetric data in standardized Talairach space," *J. Comput. Assist. Tomogr.*, vol. 18, no. 2, pp. 192–205, 1994.

[26] MNI Automated Linear Registration Package, Version 0.98, 1997 [online]. Available: ftp://ftp.bic.mni.mcgill.ca/pub/mni_autoreg/.

[27] N. Otsu, "A threshold selection method from gray-level histograms," *IEEE Trans. Biomed. Eng.*, vol. BME-9, pp. 63–66, 1979.